A&A, 710, A346 (2026)
https://doi.org/10.1051/0004-6361/202558459
© The Authors 2026

Astronomy & Astrophysics

ANAorb: A robust framework for the optimal modelling of binaries

Manuel Andrade[1,2,⋆]

[1] CITMAga, 15782 Santiago de Compostela, Galiza, Spain
[2] OARMA, Astronomy and Astrophysics Section, Department of Applied Mathematics, Faculty of Mathematics, Universidade de Santiago de Compostela, 15782 Santiago de Compostela, Galiza, Spain

Received 8 December 2025 / Accepted 12 March 2026

ABSTRACT

Context. Reliable orbital solutions for binary stars are essential for deriving accurate stellar parameters and for testing stellar-evolution models. However, current fitting approaches often struggle with local minima, strong parameter correlations, and the heterogeneous nature of historical and modern astrometric data (e.g. micrometric and interferometric). As the volume and precision of astrometry from missions such as *Gaia* grow, these limitations increasingly risk producing biased or sub-optimal orbital solutions.
Aims. We introduce a unified and statistically rigorous framework for modelling binary-star orbits that overcomes the common weaknesses of existing methods. The approach is designed to integrate heterogeneous datasets, mitigate parameter degeneracies, avoid convergence to local minima, and provide reliable and internally consistent uncertainty estimates.
Methods. We developed `ANAorb`, a flexible orbital-modelling framework that incorporates several methodological advances. These include: (i) a statistically rigorous outlier-detection and rejection scheme based on M-estimators; (ii) the combined use of multiple global and local optimisation algorithms to ensure efficient and robust convergence; and (iii) uncertainty estimation via a jackknife resampling procedure. The `ANApar` module, embedded within the workflow, provides dynamical parallaxes and individual stellar masses that are directly tied to the fitted orbit.
Results. `ANAorb` converges rapidly, typically within a few hundred iterations, and systematically improves standard goodness-of-fit diagnostics (e.g. χ^2 and rms residuals) relative to existing solutions. Outliers are removed in a statistically justified manner, and jackknife resampling yields realistic uncertainties for all parameters. Application to the benchmark systems 70 Tau (in the Hyades moving group) and 22 Cas A (a B-type emission-line star with a circumstellar envelope) demonstrates markedly improved orbital solutions, distances, and individual masses.
Conclusions. Binary systems are fundamental laboratories for stellar astrophysics. `ANAorb` provides a fast, reliable, and statistically consistent framework for deriving precise orbital solutions from heterogeneous data, while the `ANApar` module delivers accurate dynamical parallaxes and individual masses. The methodology establishes a general and reproducible framework suited to forthcoming large-scale analyses of binary-star populations.

Key words. methods: numerical – methods: statistical – astrometry – celestial mechanics – binaries: visual – stars: fundamental parameters

1. Introduction

Félix Savary was the first to compute the orbit of a visual binary star in 1827 (Savary 1830). He succeeded in fitting a Keplerian ellipse using four measurements of the angular separation, ρ, and position angle, θ, at epoch t, all obtained after the discovery of ξ Ursae Majoris on 1780 May 2 by Herschel (1803). In the years that followed, many analytical methods were developed to tackle this problem (e.g. Kowalsky 1873). However, a major milestone was reached with the Thiele-Innes-van den Bos method, which was a remarkably direct procedure. It was first proposed by Thiele (1883), inspired by Gauss's idea of using the sector minus triangle differences between three positions in the orbit computation of Ceres. The method was later modified and successfully applied to binary systems by van den Bos (1926, 1932), who used the Innes constants. It allows us to derive the orbital parameters from three observations together with the areal constant, the latter usually determined from additional measurements.

Over the years, numerous other analytical approaches have been proposed. Among the methods that directly determine the relative orbit of the system, particular mention should be made of that of Cid (1958), which does not require knowledge of the areal constant. In this method, the orbit is derived from the minimum necessary number of exact observations, namely three complete measurements $(t_j;\, \rho_j,\, \theta_j)_{j=1,2,3}$ and one incomplete measurement of the form $(t_4;\, \theta_4)$. The latter also forms the basis of the algorithm developed by Docobo (1985) for obtaining the family of Keplerian orbits passing through three observed positions.

However, the main weakness of these heuristic methods is that they do not make simultaneous use of all available observations. As a result, obtaining a plausible orbital solution relies heavily on the experience of the user. Furthermore, even under favourable circumstances, this preliminary orbit will need to be refined using differential corrections in order to yield an acceptable solution. In this context, we recall the words of Wulff Heintz regarding the Thiele-Innes-van den Bos method (equally applicable to all approaches based on only three measurements): 'Both in theoretical clarity and in practical applicability this method leaves nothing to be desired. Yet it cannot be expected to handle all possible cases. The three selected places – even when smoothed by graph or computation – may not suffice to describe the motion sufficiently' (Heintz 1978).

⋆ Corresponding author: `manuel.andrade@usc.gal`

Open Access article, published by EDP Sciences, under the terms of the Creative Commons Attribution License (https://creativecommons.org/licenses/by/4.0), which permits unrestricted use, distribution, and reproduction in any medium, provided the original work is properly cited.
This article is published in open access under the Subscribe to Open model. Subscribe to A&A to support open access publication.

In fact, orbit-determination methods based on only three measurements have become largely obsolete with the advent of numerical techniques that exploit the full set of available observations and the increasing power of modern computers. Among these contemporary approaches are grid-search techniques (Hartkopf et al. 1989), global optimisation techniques such as simulated annealing (Pourbaix 1994), the Levenberg–Marquardt algorithm (Tokovinin 2016), and Markov chain Monte Carlo algorithms (Dupuy & Liu 2017; Mendez et al. 2017). Together, these represent a wide range of powerful tools for determining the orbits of visual binaries. Indeed, several of them have been employed to derive many of the orbits included in the Sixth Catalog of Orbits of Visual Binary Stars (Hartkopf et al. 2001a), hereafter ORB6. More recently, general orbital-fitting frameworks based on Bayesian modelling have also been developed, primarily aimed at the extrasolar-planet community (Blunt et al. 2020; Brandt et al. 2021; Thompson et al. 2023).

However, this should not suggest that the determination of the optimal orbital solution is complete. With the progress in computational hardware and algorithms, it is now feasible to apply advanced global and local optimisation techniques, reinforced by parallelisation frameworks that mitigate the substantial computational cost of exploring high-dimensional parameter spaces. As a result, it becomes possible to retrieve a best-fitting orbit that – if not the precise global minimum – is expected to fall within its close neighbourhood, even when the dataset contains several hundred astrometric measurements. In addition, recent advances in robust statistical analysis have provided powerful tools for the rigorous identification of outliers, allowing the construction of more reliable datasets and, consequently, the derivation of more accurate orbital solutions.

Therefore, we present a comprehensive procedure designed to automatically perform a robust statistical analysis of observational data (classifying measurements, identifying and rejecting potential outliers, and assigning rigorous weights) as well as to determine the corresponding optimised orbital solution using a wide range of global and local optimisation algorithms. This work has culminated in the development of `ANAorb`, a Wolfram Mathematica-based framework that implements parallel programming; its workflow is described in detail in this paper. In addition, we discuss several key aspects related to the optimal computation of visual orbits and propose a set of guidelines aimed at standardising presentation practices within this classical field of astronomy. The performance of the proposed mathematical procedure is demonstrated by computing new orbits for 70 Tau and 22 Cas A, two systems of particular astrophysical interest that offer stringent tests for orbit-determination methods.

Furthermore, accurate dynamical parallaxes and individual stellar masses are also provided, as `ANApar` (Andrade 2019) is now fully integrated into `ANAorb`. In this sense, the present study can be regarded as a natural continuation of that previous work.

The paper is organised as follows. Section 2 outlines a few preliminary considerations. The optimal computation of binary orbits with `ANAorb` is presented in Sect. 3, and its application to two illustrative examples is discussed in Sect. 4. Finally, Sect. 5 summarises the main results and conclusions.

2. Previous considerations

2.1. Input data

The observational record of visually resolved binary systems is diverse and complex, chiefly due to the wide range of techniques employed over time and the varying accuracy of position measurements. Broadly speaking, two principal types of data can be distinguished: micrometric measurements, obtained with telescopes of different apertures over more than two centuries of double-star observations, and interferometric measurements, primarily those acquired through speckle interferometry with medium- and large-sized telescopes. These two datasets differ markedly in their statistical properties; in general, the former exhibit substantially larger variances than the latter. At the same time, accurate orbit determination depends critically on the reliability and sufficiency of the positional data. Nevertheless, interferometric measurements may also, on occasion, display significant deviations that could adversely affect the accuracy of the derived orbital solution. It is therefore essential to perform a robust statistical analysis of the entire dataset before proceeding with any orbital computations. These matters are discussed in detail in Sect. 3.1.

In addition, the forthcoming *Gaia* DR4 is expected to provide epoch astrometric measurements for a large number of non-single stars, thereby offering an important complement to classical micrometric and interferometric observations of binary systems. However, these data consist of one-dimensional along-scan measurements, and thus are not directly comparable to the two-dimensional differential astrometry currently treated by `ANAorb`. Their incorporation would require projection of the orbital model onto the instantaneous along-scan direction together with a reformulation of the weighting scheme. Although the robust deterministic optimisation framework of `ANAorb` is well suited to heterogeneous and irregular data, extending the present implementation to include *Gaia* DR4 data lies beyond the scope of this work and is therefore deferred to future developments.

2.2. The Keplerian model

The orbit of a visual binary star is described by seven parameters, commonly referred to as the orbital elements. The standard set of elements defining the motion of the secondary relative to its primary component are the Campbell elements (P, T, e, a, i, Ω, and ω) where P is the orbital period (in years or days), T is the epoch of periastron passage (in years), e is the eccentricity, a is the semi-major axis of the true orbit (in arcseconds), i is the inclination (in degrees), Ω is the position angle of the ascending node, referred to the J2000.0 equinox (in degrees), and ω is the longitude of periastron (in degrees), measured from the ascending node. Further details are provided in Appendix A.

For each binary system, the orbital elements are determined from the full set of n relative astrometric observations. These measurements are expressed as polar coordinates $(t_j;\, \rho_j,\, \theta_j)_{j=1\ldots,n}$, where t_j denotes the time of observation.

3. Robust computation of optimised orbits

This section outlines the workflow implemented in `ANAorb` to compute optimised orbital solutions, combining robust statistical techniques with optimisation methods designed to explore the parameter space and approach the global minimum associated with the best-fitting orbital elements of a given binary system.

3.1. Robust analysis

Accurate orbit determination requires verification of three key assumptions: (1) the residuals (observed minus predicted orbital positions) should exhibit no systematic trends (i.e. errors are independent); (2) the scatter of the residuals should remain

constant throughout the orbit (homoscedasticity); and (3) the residuals should follow a normal distribution. Violations of these assumptions may indicate the presence of measurement biases or un-modelled perturbations (e.g. third-body effects).

3.1.1. Detecting outliers: The outlier map

Nevertheless, the observational dataset of a binary system often contains outliers, that is, position measurements that deviate significantly from the expected values, exhibiting moderate or large residuals. If not properly identified and handled, such anomalous data points can lead to substantial errors in the derived orbital elements. This task, however, must be undertaken with care, as it is well known that classical approaches to outlier detection, based on standard influence measures (e.g. the Mahalanobis distance, MD hereafter), may suffer from two well-documented issues: masking and swamping. The former occurs when an outlier goes undetected, while the latter arises when a non-outlier is incorrectly classified as one.

To mitigate these problems, `ANAorb` implements a robust and computationally efficient method proposed by Rousseeuw & van Zomeren (1990) to detect outliers and to prevent the elimination of observations containing significant information. Their approach involves constructing an outlier map, in which the robust residuals are plotted against the robust distances (RDs). The residuals are obtained using a robust regression estimator, such as the least median of squares (LMS), defined by Rousseeuw (1984) as the solution to the minimisation problem

$$\min_{\hat{\xi}} \underset{j=1,\ldots,n}{\text{median}}\, r_j^2\left(\hat{\xi}\right), \tag{1}$$

where $r_j(\hat{\xi}) = y_j - \mathbf{x_j}\,\hat{\xi}$ is the residual of the j^{th} observation and $\hat{\xi}$ the LMS estimate that is affine equivariant and has the maximal breakdown point, thus ensuring both invariance with respect to coordinate transformations and maximal robustness against outliers. Hence, the standardised LMS residuals are given by $\bar{r}_j = \dfrac{r_j}{\hat{\sigma}}$, $\hat{\sigma}$ being the corresponding scale estimate (Rousseeuw & Leroy 1987).

On the other hand, rather than using the classical MDs, we employ RDs computed from robust estimates of location and scatter (covariance). Rousseeuw & van Zomeren (1990) calculated RDs using the minimum volume ellipsoid method, but the minimum covariance determinant (MCD) estimator proposed by Rousseeuw (1985) has been shown to be more efficient. In this work, RDs are derived by means of the FAST-MCD algorithm proposed by Rousseeuw & Driessen (1999). Robust estimators are designed to achieve both high robustness (being less influenced by outliers) and high efficiency (remaining precise for uncontaminated data).

Finally, an outlier map (or diagnostic plot) is generated, plotting the standardised LMS residuals versus the MCD-derived RDs and indicating the cutoff thresholds for both quantities (± 2.5 for the residuals and $\sqrt{\chi^2_{p,0.975}}$, with p degrees of freedom, for the distances), as shown in Fig. 1. This diagnostic plot allows us to identify four types of observations in the dataset: regular observations (small $|\bar{r}_j|$ and small RD_j), vertical outliers (large $|\bar{r}_j|$ and small RD_j), good leverage points (small $|\bar{r}_j|$ but large RD_j), and bad leverage points (large $|\bar{r}_j|$ and large RD_j). As a rule of thumb, bad leverage points and vertical outliers are removed from the dataset.

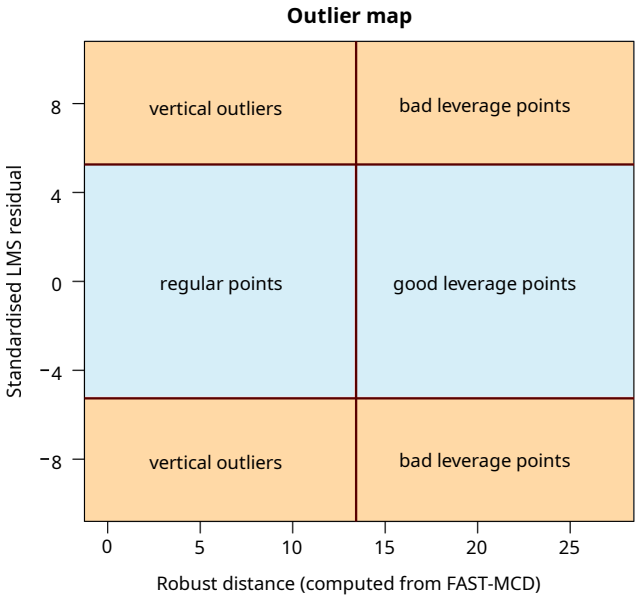

Fig. 1. Outlier map used to identify regular points and good leverage points (light blue) versus vertical outliers and bad leverage points (light orange).

3.1.2. The weighting procedure

The usual approach to assigning weights involves using the inverse of the individual variance associated with each measurement. However, as the publication of such variance values is not customary, many authors have traditionally assigned weights to observations by alternative means. In this context, Hartkopf et al. (1989, 2001a) proposed a weighting scheme (updated in September 2017) based on both objective and subjective factors.

Nevertheless, given that the assignment of relative weights is a tricky task that can strongly affect the final results, and with the aim of making this otherwise necessary procedure as simple and robust as possible, we adopt the following straightforward approach:

(i) Initial weights:

The initial weight for each j measurement is calculated, considering only objective factors, as

$$w_j^0 = w_t\, w_d\, w_n\, w_q, \tag{2}$$

where w_t is the relative weight for a given class of technique, w_d is the relative weight taking into account the size of the telescope, w_n is the relative weight considering the number of observations to obtain a measurement, and w_q is a factor that estimates the quality of each measurement depending on whether it was flagged as being uncertain or of poor quality (see Table 1). In any case, it should be noted that simply adopting $w_j^0 = 1$ usually works well, although it may prove problematic in situations where only a few measurements are available and some of them are affected by large errors.

(ii) Re-weighting:

In the subsequent stages, after detecting and removing vertical outliers and bad leverage points from the dataset, new robust weights are computed before calculating the orbital elements at each stage. The first stage is to check that the cleaned dataset follows a normal distribution, using the well-known tests of Shapiro & Wilk (1965) and Jarque & Bera (1981) at a significance level of $\alpha = 0.05$, together with inspection via a normal Q-Q plot.

Table 1. Factors for determining initial weights.

Factor	Value	Type
w_t	1.00	Interferometric
	0.05	Micrometric
w_d	D^2	
	D	Long-baseline interferometry
w_n	$\sqrt{n}$	
w_q	1.0	Normal accuracy
	0.5	Low accuracy

Notes. The telescope diameter is denoted by D and expressed in metres, while n denotes the number of observations used to obtain a measurement.

The procedure combines several robust estimation techniques, employing weighting functions based on the Tukey, Huber, and Welsch estimators.

Thus, if the measurements exhibit a normal distribution, as expected after having eliminated potential outliers, the Huber weights are applied:

$$w_H(r_j) = \min\left\{1, \frac{c_H}{|r|}\right\}, \tag{3}$$

where c_H is a tuning constant. A higher value of c_H increases efficiency but reduces robustness to outliers, whereas a lower value decreases efficiency while improving robustness. The default value for standardised residuals is usually $c_H = 1.345$, which correspond to a high asymptotic efficiency of 95% for normally distributed data and provides a good balance between robustness and efficiency.

On the contrary, if the dataset remains non-normal after the removal of outliers and bad leverage points, or displays a heavy-tailed distribution, the Tukey bi-square weights are employed:

$$w_H(r_j) = \left[\max\left\{0, 1 - \left(\frac{r}{c_T}\right)^2\right\}\right]^2, \tag{4}$$

where $c_T = 4.685$ corresponds to an asymptotic efficiency of 95% for a normal population.

For intermediate cases in which the normality tests yield inconclusive results, the Welsch weights are adopted:

$$w_W(r_j) = e^{-\left(\frac{r}{c_W}\right)^2}, \tag{5}$$

where $c_W = 2.985$ corresponds to an asymptotic efficiency of 95% for a normal population.

3.2. Formulation of the minimisation problem

3.2.1. The objective function

The computation of the orbit is formulated as a mathematical optimisation problem in which the objective function to be minimised depends on the orbital elements. The goal is therefore to determine the solution to the minimisation problem defined as

$$\min_{\mathbf{v}\in V} \mathcal{J}(\mathbf{v}), \tag{6}$$

where $\mathcal{J} : \mathbb{R}^7 \longrightarrow \mathbb{R}$ is the objective function, and V denotes the search space defined by the set of the orbital elements according to

$$\begin{aligned} V = \{\mathbf{v} \in \mathbb{R}^7 : & 0 < P < \infty,\ -\infty < T < \infty,\ 0 \le e < 1, \\ & 0 < a < \infty,\ 0 \le i \le \pi,\ 0 \le \Omega < 2\pi, \\ & 0 \le \omega < 2\pi\}. \end{aligned} \tag{7}$$

As usual, we consider the chi-squared (χ^2) statistic to evaluate the goodness of fit between the data and our model. Traditionally, this evaluation has been based on the differences between the observed and calculated polar coordinates (namely, the angular separation and position angle) as indicators of orbital accuracy. However, this approach is not ideal for comparing orbital solutions, since errors in polar coordinates are inherently correlated due to the nature of the measurement process. To overcome this limitation, we propose to use the Euclidean distance (based on the L_2 norm), computed from Cartesian coordinates in the apparent orbital plane, as the optimal metric for quantifying similarity between the observed $\mathbf{x} = (x_j, y_j)$ and the calculated $\bar{\mathbf{x}}(\mathbf{v}) = (\bar{x}_j(\mathbf{v}), \bar{y}_j(\mathbf{v}))$ points. That is,

$$d_2(\mathbf{x}, \bar{\mathbf{x}}(\mathbf{v})) := \|\mathbf{x}, \bar{\mathbf{x}}\|_2 = \sqrt{(\mathbf{x} - \bar{\mathbf{x}})^T(\mathbf{x} - \bar{\mathbf{x}})},\ \text{for } \mathbf{x}, \bar{\mathbf{x}} \in \mathbb{R}^2. \tag{8}$$

Therefore, the maximum-likelihood estimate of the model parameters is obtained by minimising the quantity

$$\begin{aligned} \mathcal{J}(\mathbf{v}) &= \sum_{j=1}^{n} \frac{w_j}{w}\, d_2^2(\mathbf{x}, \bar{\mathbf{x}}(\mathbf{v})) \\ &= \sum_{j=1}^{n} \frac{w_j}{w} \left[(x_j - \bar{x}_j(\mathbf{v}))^2 + (y_j - \bar{y}_j(\mathbf{v}))^2\right], \end{aligned} \tag{9}$$

where $w = \sum_{j=1}^{n} w_j$ is the sum of the partial weights.

Therefore, after removing vertical outliers and bad leverage points via LMS residuals and MCD RDs, the orbital fit is performed using an iteratively re-weighted least squares scheme based on classical M-estimators (Huber, Tukey, and Welsch), ensuring robust parameter estimation.

3.2.2. Additional constraints

Additionally, certain constraints on the search space of the orbital elements can be taken into consideration when complementary information is available. For instance, one might restrict the search to orbits with periods shorter than a specified value. In this way, the search space (V) defined in Eq. (7) can be replaced by a more constrained space:

$$\begin{aligned} V_c = \{\mathbf{v} \in \mathbb{R}^7 : & P_{min} \le P \le P_{max},\ T_{min} \le T \le T_{max}, \\ & e_{min} \le e \le e_{max},\ a_{min} \le a \le a_{max}, \\ & i_{min} \le i \le i_{max},\ \Omega_{min} \le \Omega \le \Omega_{max}, \\ & \omega_{min} \le \omega \le \omega_{max}\}. \end{aligned} \tag{10}$$

This is particularly useful when a well-constrained spectroscopic orbit has already been determined. Although the current implementation of `ANAorb` is designed as a pure astrometric solver and does not perform a simultaneous joint fit of radial velocities and astrometric measurements, spectroscopic information can nevertheless be incorporated in a practical manner. In such cases, spectroscopic orbital elements (P, T, e, and ω) and their

associated uncertainties can be used to constrain the explored parameter space, thereby restricting the optimisation to the subspace defined by the spectroscopic solution. This approach yields orbital solutions that remain consistent with both the relative astrometry and the existing radial velocity constraints, while preserving the robustness of the astrometric fit.

Furthermore, if the parallax and the apparent magnitudes are known, the minimisation problem can be subject to the following inequality constraints on the orbital elements P and a, derived from Kepler's third law:

$$\begin{cases} C_1(P,a) = \dfrac{a^3}{\varpi^3\, P^2} - \mathcal{M} - \delta\mathcal{M}^{\rm inf} \;\leq\; 0, \\ C_2(P,a) = \dfrac{a^3}{\varpi^3\, P^2} - \mathcal{M} + \delta\mathcal{M}^{\rm sup} \;\geq\; 0, \end{cases} \tag{11}$$

where ϖ is the parallax, $\mathcal{M}$ is the system mass, and $\delta\mathcal{M}^{\rm inf}$ and $\delta\mathcal{M}^{\rm sup}$ are the lower and upper admissible limits, respectively, with respect to the system mass.

As previously noted, the parallax can be taken from *Gaia*, or otherwise from HIPPARCOS. Regarding the systems mass, we suggest to take $\delta\mathcal{M}^{\rm inf} = \delta\mathcal{M}^{\rm sup} = \Delta \cdot u(\mathcal{M})$, where $u(\mathcal{M})$ is the uncertainty in the system mass and Δ is a coverage factor, typically in the range 1 to 5, which is chosen according to the desired level of confidence. `ANAorb` allows the system mass $\mathcal{M}$ to be estimated from the photometric calibration of Pecaut & Mamajek (2013) for main-sequence stars, or alternatively from those of Xia & Fu (2010) for stars with $0.60\,\mathcal{M}_\odot < \mathcal{M} < 22.89\,\mathcal{M}_\odot$ and Benedict et al. (2016) for those with $0.08\,\mathcal{M}_\odot < \mathcal{M} \leq 0.60\,\mathcal{M}_\odot$. Photometric masses of subgiant, giant, and supergiant stars are instead estimated using the calibrations of Straizys & Kuriliene (1981).

On the other hand, the interstellar extinction can be estimated using the classical exponential law of Parenago (1945), adopting the parametrisation of Sharov (1964), which provides an analytical approximation of the extinction. Nevertheless, for improved accuracy, `ANAorb` also supports the use of distance-dependent extinction values derived from three-dimensional dust maps, based on line-of-sight integrated estimates, such as those provided by the EXPLORE/G-Tomo service (Lallement et al. 2022). This approach enables target-specific extinction corrections and is particularly relevant for the `ANApar` module, where photometric information is incorporated and reliable de-reddening is required.

Consequently, the constraints expressed in Eq. (11) restrict the feasible solutions to those orbits corresponding to physically realistic masses. However, it should be borne in mind that these constraints will work reasonably well only when both the parallax and the apparent magnitudes are known with sufficient accuracy. As general rule, and in agreement with van Leeuwen (2007), these constraints should not be applied if the relative uncertainty in the parallax exceeds 10 percent.

3.2.3. Initial point

Algorithms for unconstrained minimisation require a starting point, which we denote by $\mathbf{v}_0$. Beginning from this point, optimisation algorithms generate a sequence of iterates, $\{\mathbf{v}_k\}_{k=1}^{n}$, which terminates when no further progress can be achieved or when a solution is deemed to have been approached with sufficient accuracy.

`ANAorb` can be configured to initiate its search from one or more specified starting points. When no prior preference is available, one can take advantage of the known values of the system mass and parallax. In such cases, we propose the initial choice

$$\begin{cases} a_0 = \max\{\rho_j\}, \;\; \text{with } j = 1, \ldots, n, \\ P_0 = \sqrt{\dfrac{a_0^3}{\mathcal{M}\,\varpi^3}}, \\ \text{along with random } T_0,\; e_0,\; i_0,\; \Omega_0,\; \text{and } \omega_0, \end{cases} \tag{12}$$

where $\mathcal{M}$ is obtained from the aforementioned photometric calibrations.

Alternatively, `ANAorb` can be configured to generate an arbitrary population of random starting points. A local optimisation method is then applied to each point to locate its corresponding local minimiser, and the best among these solutions is adopted as the final result. `ANAorb` also allows us to specify the local optimisation algorithm, as well as other key parameters such as the number of starting points $N_{\rm sp}$ and their coordinates.

3.2.4. The suite of local and global methods

The purpose is to find the global minimiser $v^* \in V$ (or V_c) such that

$$\mathcal{J}(\mathbf{v}^*) \leq \mathcal{J}(\mathbf{v}), \;\; \forall\, \mathbf{v} \in V,$$

or failing that, to find the local minimiser given by the best local solution with respect to the ϵ-neighbourhood of a point $\mathbf{v}^* \in V$, that is, V_ϵ, such that

$$\mathcal{J}(\mathbf{v}^*) \leq \mathcal{J}(\mathbf{v}), \;\; \forall\, \mathbf{v} \in V_\epsilon(\mathbf{v}^*) \text{ with } \epsilon > 0.$$

This task is accomplished through the use of global and local optimisation methods implemented in `ANAorb` using parallel computing. The global methods include direct-search algorithms that do not rely on derivative information and aim to locate the global minimum. The local methods, by contrast, comprise either gradient-based or derivative-free algorithms that, when convergent, identify local minima (or even the global minimum). In some cases, the search space is further reduced by treating the problem as constrained, as expressed in Eqs. (10) and (11). Additional details on the fundamental concepts, together with a brief description of the methods and parameters controlled by `ANAorb`, are provided in Appendix B.

3.2.5. The three-stage resolution scheme

Once the initial weights have been assigned to the observational dataset, the optimisation strategy proposed in this work for obtaining the statistically most favourable local minimum (and potentially the global minimum) of the model's objective function proceeds through the following three stages:

Stage 1. We first solve the optimisation problem, Eq. (6). In the absence of a previously known orbit, a multi-start random-search strategy is employed. When a prior solution is available, a combination of global and local optimisation algorithms is used instead. This stage provides a preliminary orbital estimate.

Stage 2. The preliminary orbit is then used to perform a first robust re-weighting of the observations. With these revised weights, the suite of global and local optimisation methods is applied again to obtain an improved initial orbit.

Stage 3. The initial orbit forms the basis for a second robust re-weighting, from which the outlier map is constructed and any outliers are identified and removed. A final application of the optimisation methods then yields the final orbital solution.

3.3. Uncertainties: The jackknife procedure

The determination of the uncertainties associated with each orbital element is often a complex task that does not always satisfy the requirement for a rigorous characterisation of the quality of an orbit. Even today, a number of orbit determinations are derived using rather ad hoc or intuitive estimates.

To address this issue, we propose the use of a weighted (delete-1) jackknife variance estimator to compute the standard uncertainties and confidence intervals of the orbital elements. This is a well-established and robust technique, independent of model assumptions and well suited to parallel computation. The jackknife method was originally developed by Quenouille (1949) to estimate the bias of an estimator and was later extended by Tukey (1958) to include variance estimation, who also introduced its current name.

The estimator of the orbital element v based on the n measurements $x_1, \ldots, x_n$ is denoted by $\widehat{v}$, so that

$$\widehat{v} = \widehat{v}(x_1, \ldots, x_n). \tag{13}$$

Removing the j-th observation from the dataset yields the partial estimate

$$\widehat{v}_j = \widehat{v}_j(x_1, \ldots, x_{j-1}, x_{j+1}, \ldots, x_n), \tag{14}$$

and the corresponding j-th pseudo-value of $\widehat{v}$ then reads

$$\widehat{v}_j^* = n\widehat{v} - (n-1)\widehat{v}_j. \tag{15}$$

Pseudo-values can thus be interpreted as a bias-correction version of $\widehat{v}$. The Quenouille's jackknife estimator of v, denoted v^*, is defined as the average of the pseudo-values

$$\widehat{v^*} = \frac{1}{n}\sum_{j=1}^{n}\widehat{v}_j^*. \tag{16}$$

The weighted jackknife variance estimator is then defined as

$$[\sigma^*(\widehat{v})]^2 = \frac{1}{n-1}\,\frac{\sum_{j=1}^{n} w_j^{-1}\left(\widehat{v}_j^* - \widehat{v^*}\right)^2}{\sum_{k=1}^{n} w_k^{-1}}. \tag{17}$$

This is considered a good estimator of $[\sigma(\widehat{v})]^2$ (Hinkley 1978; Efron 1982). For large n, the jackknife estimate is approximately normally distributed about the true parameter v. Hence, the standard uncertainty of the mean of each orbital element v is given by

$$u(v) = \sqrt{\frac{[\sigma^*(\widehat{v})]^2}{n}}. \tag{18}$$

Likewise, the confidence interval can be expressed as

$$CI_{1-\alpha} = t_{1-\alpha/2,n-1}\; u(v), \tag{19}$$

where $t_{1-\alpha/2,n-1}$ is the Student's t-distribution with α being the level of significance. In this way, `ANAorb` provides both the standard uncertainties and the confidence intervals associated with the derived orbital elements.

It should be noted that, for sufficiently smooth $\widehat{v}$, the consistency and asymptotic unbiasedness of the delete-1 jackknife variance can be demonstrated (Shao & Wu 1989). Nevertheless, when computing the jackknife estimate, it is advisable to inspect the variability of $\left(\widehat{v}_j^* - \widehat{v}^*\right)$ to detect any potential outliers.

Finally, the uncertainties are rounded, as usual, to two significant figures, and the orbital elements are reported with the same number of decimal places as their corresponding uncertainties. In a few cases, however, it is necessary to retain additional digits to avoid round-off errors in subsequent calculations (for example, when computing future epochs of periastron passage).

3.4. Evaluation of an orbit

In the context of orbit determination, accuracy encompasses two complementary aspects: trueness and precision. Trueness characterises the degree to which an orbital solution is free from systematic bias and reflects how faithfully the derived orbit represents the underlying physical configuration given the available observational constraints. Precision, by contrast, quantifies the level of random uncertainty and describes the internal consistency of the fitted solution as inferred from the scatter of the residuals and the associated statistical uncertainties. A solution may therefore be unbiased yet poorly constrained, or conversely highly precise but affected by systematic bias. A meaningful assessment of orbital quality thus requires the joint evaluation of both trueness and precision, which together define the global accuracy of an orbital solution.

From an operational standpoint, the reliability of the observational data is characterised by the number of measurements and the uniformity of their distribution over the orbital period. The internal consistency of the inferred orbital elements and the corresponding model predictions is assessed independently through the associated uncertainty estimates and the value of the objective function at the attained minimum.

3.4.1. Trueness

It is essential to have a comprehensive and reliable set of measures. To characterise these properties, we define a new factor, the 'normalised factor of trueness' (Φ), which depends on the following normalised dimensionless parameters:

Orbital coverage ($0 \le \delta \le 1$): This factor gives the extent of the orbital arc covered by measurements. In practice, it depends solely on the measurements and attains its maximum value when the observed arc spans one full orbital period or more. We define it as

$$\delta\,(P; t_1, t_n) = \begin{cases} \mathrm{frac}\left(\dfrac{t_n - t_1}{P}\right), & \text{if } t_n - t_1 < P, \\ 1, & \text{if } t_n - t_1 \ge P, \end{cases} \tag{20}$$

where $\mathrm{frac}\,(z)$ is the fractional part of z. The quantities t_1 and t_n correspond to the epochs of the first and last measurements, respectively.

Dispersion of measures ($0 \le \lambda \le 1$): This factor describes the dispersion of the measurements along the orbit, reaching its maximum value when the measurements are evenly distributed. First, to compute it, we consider the set of arc lengths between two consecutive measurements x_i and x_j

$$S = \left\{ \ell\left(x_i, x_j\right)_{i<j} \right\}, \tag{21}$$

and compute the total length of the orbital ellipse, $L(e, a, i)$. Thereafter, we retain those arc lengths exceeding a prescribed threshold, which, as a rule of thumb, is set to one-twentieth of the total length of the ellipse:

$$S^* = \left\{ \ell \in S \mid \ell > \frac{L}{20} \right\}. \tag{22}$$

Therefore,

$$\lambda(e, a, i, \Omega, \omega; \Delta\theta_j^*) = \frac{L - \sum_{\ell^* \in S^*} \ell^*}{L}, \tag{23}$$

where $\Delta\theta_j^* = \theta_{j+1} - \theta_j$ is the angular separation between two consecutive measurements.
Consequently, the expression used to compute the normalised factor of trueness is the geometric mean, given by

$$\Phi = \sqrt{\delta\,\lambda}, \quad \text{with } 0 \le \Phi \le 1. \tag{24}$$

The normalised factor of trueness is determined by the observational data. Therefore, it quantifies the goodness of the measurements but contains no information about the quality or validity of the orbital computation.

3.4.2. Precision

On the other hand, it is also necessary to evaluate the precision of the derived orbital elements. To this end, we define a new factor, the 'normalised factor of precision' (Θ), which depends on the following normalised and dimensionless parameters:
Orbital precision ($0 \le \epsilon \le 1$): we propose the following function as a global quantitative measure of the precision of the orbit

$$\epsilon\,(P, T, e, a, i, \Omega, \omega) = \begin{cases} \min\limits_{1 \le k \le 7} [1 - u_r(v_k)], & \text{if } u_r < 1\ \forall\, v_k, \\ 0, & \text{if } \exists\, v_k : u_r \ge 1, \end{cases} \tag{25}$$

$u_r(v_k)$ being the normalised relative uncertainty of each orbital element v_k. When the uncertainties of the orbital elements are unavailable, this parameter cannot be determined and we consequently adopt $\epsilon = 0$.

Orbital correlation ($0 \le \beta \le 1$): this factor quantifies the orbital correlation through the following function of the minimum value of the objective function

$$\beta\left(P, T, e, a, i, \Omega, \omega; t_j\right) = \frac{1}{1 + \sqrt{\dfrac{\mathcal{J}(\mathbf{v}^*)}{a^2}}}, \tag{26}$$

where v^* is the set of orbital elements that minimises the objective function defined in Sect. 3.2.1.

Consequently, the expression used to compute the normalised factor of precision is the geometric mean given by

$$\Theta = \sqrt{\epsilon\beta}, \quad \text{with } 0 \le \Theta \le 1. \tag{27}$$

This factor contains all relevant information on how well the computed orbital elements match the observations, as determined by the minimisation function. In fact, as the normalised precision factor is entirely set by the optimisation scheme adopted to compute the orbital elements, it serves as an indicator of the internal consistency and precision of the orbital solution.

Table 2. Evaluation scheme for the index of accuracy, Γ.

Γ	Evaluation	Grade
[0.95, 1.0]	Validated	1
[0.90, 0.95)	High confidence	2
[0.85, 0.90)	Well constrained	3
[0.80, 0.85)	Reliable	4
[0.7, 0.8)	Moderately constrained	5
[0.6, 0.7)	Provisional	6
[0.5, 0.6)	Preliminary	7
[0.4, 0.5)	Uncertain	8
[0.3, 0.4)	Low confidence	9
[0.0, 0.3)	Invalid	10

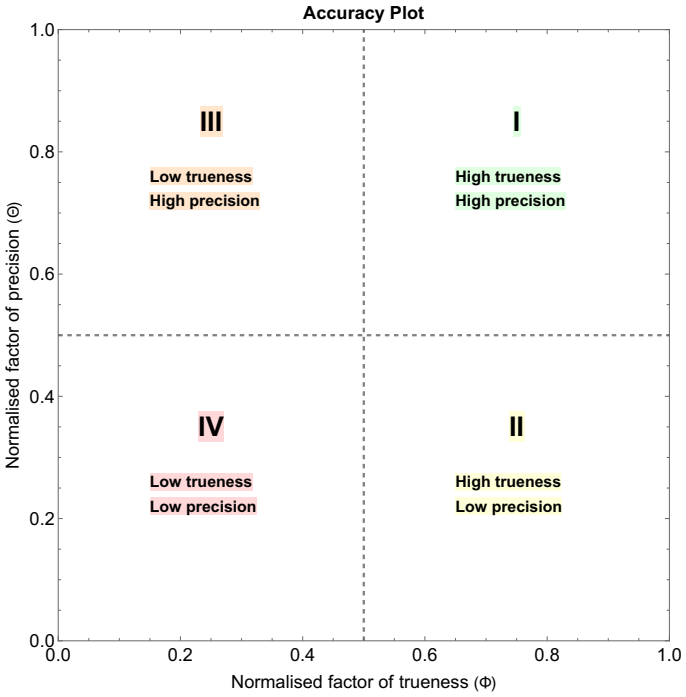

Fig. 2. Accuracy plot illustrating the four orbital categories defined by the normalised trueness and precision factors of the orbit.

3.4.3. Assessing global accuracy

Moreover, both the normalised factor of trueness (Φ) and the normalised factor of precision (Θ) can be used to construct a diagram that enables the accuracy of orbits from different systems to be visualised and compared. In this context, we define the 'index of accuracy' of an orbit as the quadratic mean:

$$\Gamma = \sqrt{\frac{\Phi^2 + \Theta^2}{2}}, \quad \text{with } 0 \le \Gamma \le 1. \tag{28}$$

In general, the evaluation scheme outlined in Table 2 can be adopted. Furthermore, a two-dimensional plot showing the values of Φ, Θ, and Γ can be drawn for a set of orbits (see Fig. 2). This can be useful for comparing the orbits of different binary systems in terms of their accuracies.

This classification scheme provides a quantitative basis for assessing the statistical reliability of different orbital solutions through the accuracy index. Grades 1–5 correspond to scientifically robust orbits that are fully suitable for publication

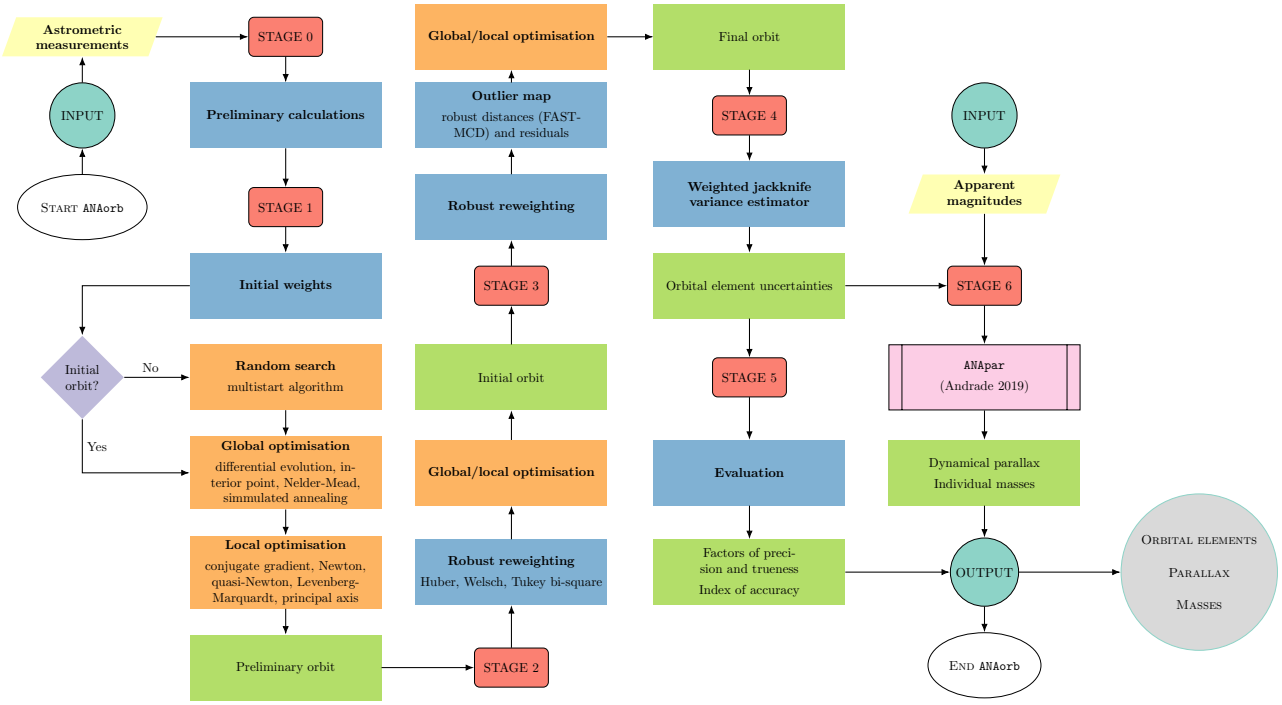

Fig. 3. Flowchart illustrating the main workflow of the `ANAorb` (`+ANApar`) framework. Further details are provided in Sect. 3.

and inclusion in catalogues. Grades 6–7 represent intermediate-quality solutions that, while not definitive, remain adequate for trend analysis or provisional compilations. In contrast, Grades 8–10 denote low-reliability or potentially spurious solutions that should be regarded as uncertain and may require additional observations or complete reanalysis.

3.5. Dynamical parallaxes and individual masses

The system mass can be derived from the trigonometric parallax provided by *Gaia* or HIPPARCOS. The orbital period and semi-major axis used in this derivation would be those obtained by `ANAorb` from the minimisation problem described in Sect. 3.2.

Nevertheless, since trigonometric parallaxes may be affected by several factors, notably the orbital motion itself, we instead propose to adopt the more accurate dynamical parallaxes and individual component masses computed using the analytical non-linear theory `ANApar` (Andrade 2019), which has been fully implemented in `ANAorb`. The entire procedure described in Sect. 3 is summarised in the flowchart presented in Fig. 3.

We fully endorse the key recommendations of Tokovinin (2024), whose work established essential guidelines for the treatment of visual binary data. In particular, we reaffirm that (a) 'when accurate (speckle or other) data are available, the old visual measures should not be used' (except in justified cases), and that (b) 'when both visual and speckle measures are used, they must be weighted according to their real errors'. The present study not only adheres to these principles but also extends them through the development of a comprehensive and fully automated robust weighting framework (Sect. 3.1.2), thereby providing a rigorous statistical foundation for the homogeneous and reliable computation of visual binary orbits.

4. Illustrative applications of the new framework

The complete procedure, including intermediate results, is presented for the well-studied binaries 70 Tau (FIN 342Aa,Ab) and 22 Cas A (NOI 3Aa,Ab). As innovative elements of the present implementation, `ANApar` adopts specific calibrations for F-type stars in the case of 70 Tau and for B-type stars in the case of 22 Cas A, and uses extinction estimates based on the 3D Galactic dust maps of Lallement et al. (2022).

4.1. Case 1: 70 Tau (FIN 342Aa,Ab/WDS 04256+1556)

This F7 V star is a double-lined spectroscopic binary that was visually resolved by Finsen (1959) and named FIN 342Aa,Ab. It is a confirmed member of the Hyades moving group (vB 57) as well.

The orbit presented in this paper was computed using measurements obtained from a variety of sources. Interferometric observations were drawn from the Fourth Catalog of Interferometric Measurements of Binary Stars (Hartkopf et al. 2001b) and from Mason & Hartkopf (2026), as well as from observational runs carried out at the Southern Astrophysical Research Telescope (Tokovinin et al. 2018, 2019, 2022) and at the Lowell Discovery Telescope (Horch et al. 2021). Micrometric measurements were taken from the Site Informatique des étoiles Doubles de Nice (Le Contel et al. 2001). In addition, numerous micrometric observations were compiled from individual publications by various observers. Many of these measurements have not previously been used for orbit computation. Thus, the orbit presented here is based on newly acquired data.

4.1.1. Robust analysis: Outliers and leverage points

The time span covered by the 8 micrometric measurements and the 99 interferometric (visual and speckle) and occultation measurements extends over ten orbital revolutions. However, only a single observation near to periastron, obtained by Hartkopf et al. (1992) and flagged as of lower accuracy, is available.

Nevertheless, as this system has been repeatedly observed since the epoch of that orbital determination, and owing to the wide variety of measurement types available, it represents an

Table 3. Optimised orbital solutions and derived parameters for FIN 342Aa,Ab and NOI 3Aa,Ab obtained with `ANAorb` (`+ANApar`).

	FIN 342Aa,Ab			NOI 3Aa,Ab		
Orbital elements						
P (yr)	6.27262	±	0.00024	2.849	±	0.034
T	2026.35830	±	0.00079	2027.043	±	0.024
e	0.71169	±	0.00054	0.028	±	0.015
a (mas)	100.12	±	0.12	17.091	±	0.039
i (deg)	124.162	±	0.069	115.24	±	0.44
$\Omega_{\rm asc}$ (deg)	215.702	±	0.083	268.74	±	0.28
ω (deg)	93.165	±	0.051	109.9	±	3.4
Dynamical parameters						
ϖ (mas)	21.823	±	0.046	3.622	±	0.043
d (pc)	45.823	±	0.097	276.1	±	3.3
$\mathcal{M}_1$ ($\mathcal{M}_\odot$)	1.2661	±	0.0076	9.97	±	0.16
$\mathcal{M}_2$ ($\mathcal{M}_\odot$)	1.1880	±	0.0079	2.98	±	0.11
q ($\equiv \mathcal{M}_2/\mathcal{M}_1$)	0.9383	±	0.0084	0.299	±	0.012
a (au)	4.588	±	0.011	4.719	±	0.057
Absolute magnitudes						
M_1 (mag)	+3.617	±	0.030	−2.69	±	0.05
M_2 (mag)	+3.957	±	0.030	+0.21	±	0.11

excellent test case for the procedure presented in this work. In fact, acting as a statistical razor, the robust analysis rejects all data observations identified as bad leverage points (43 measurements) or vertical outliers (none), retaining only those classified as good leverage points (2 measurements) or regular observations (62 measurements) for orbit computation.

As expected, most of the rejected data correspond to micrometric observations (the whole dataset, 1961–1989), visual interferometric measurements (the whole dataset, 1959–1969), the complete set of lunar occultation measurements (1978–1980), and a few speckle interferometric measurements (1978–1997). Consequently, 64 interferometric measurements (1975–2021) were ultimately used to compute the orbital elements, which are concentrated in the compact region located in the lower-left part of the outlier map shown in Fig. C.1.

4.1.2. New orbital elements

The currently adopted orbit of Fin 342Aa,Ab (Söderhjelm 1999) is classified as 'definitive' in the ORB6. Nevertheless, the orbit derived in this work achieves substantially better agreement with the observations.

We calculated new orbital elements, which are given in Table 3. In this case, the ascending node can be identified due to its spectroscopic feature. This optimised apparent orbit is shown in Fig. 4.

In terms of accuracy, this orbit yields lower mean absolute error (MAE) and root mean square error (RMSE) values for the Euclidean distance, as well as for θ and ρ, as shown in Table C.1. Furthermore, according to the new dimensionless factors proposed in this work to assess global accuracy (see Sect. 3.4), the orbit can be regarded as well constrained ($\Gamma = 0.8541$), although some room for improvement remains. In particular, additional observations around periastron would be valuable. In any case, the residuals of the new orbit are significantly reduced compared with those of the previous solution.

4.1.3. Dynamical parallax and individual masses

The combined mean G magnitude listed in the *Gaia* DR3 catalogue for this system is 6.3416 ± 0.0028, whereas the magnitude difference between the components, obtained by McAlister et al. (1988) using speckle interferometry, is 0.34 ± 0.06. From these values, the individual component magnitudes can be estimated as 6.94 ± 0.03 and 7.28 ± 0.03. The precision of these magnitudes, together with the accurately determined orbital period and semi-major axis, allows for robust estimates of the dynamical parallax and the individual component masses to be derived using `ANApar` (see Table 3).

The resulting dynamical parallax, 21.823 ± 0.046 mas, is slightly higher than the most recent trigonometric parallax reported by *Gaia* DR3, 21.11 ± 0.50 mas, with a RUWE of 24. Among the orbital parallaxes derived from radial velocities, Torres et al. (1997) obtained 21.44 ± 0.67 mas, while Griffin (2012) derived 22.58 ± 0.22 mas. The updated orbital parallax, which we also derive as 21.89 ± 0.36 mas, is fully consistent with our dynamical parallax.

This apparent underestimation of the *Gaia* trigonometric parallax may be due to contamination by the orbital motion, as already suggested by Andrade (2019), and also by Malkov & Sachkov (2025) for distant binary systems. Indeed, the distance derived in this work agrees rather well with the recent estimate of 46.09 ± 0.73 pc by Reino et al. (2018), based on *Gaia* DR1 *Tycho-Gaia* Astrometric Solution (TGAS) data for 200 members located in the central region of the Hyades cluster.

The inferred individual masses and absolute magnitudes correspond to two main-sequence stars of spectral types F6 and F8 (see Table 3), in good agreement with the combined spectral type F7 V reported by Gray et al. (2001). Moreover, they also match closely the component masses predicted by the calibrations of Xia & Fu (2010) and Pecaut & Mamajek (2013), namely 1.27 and 1.19 $\mathcal{M}_\odot$, respectively, in both cases.

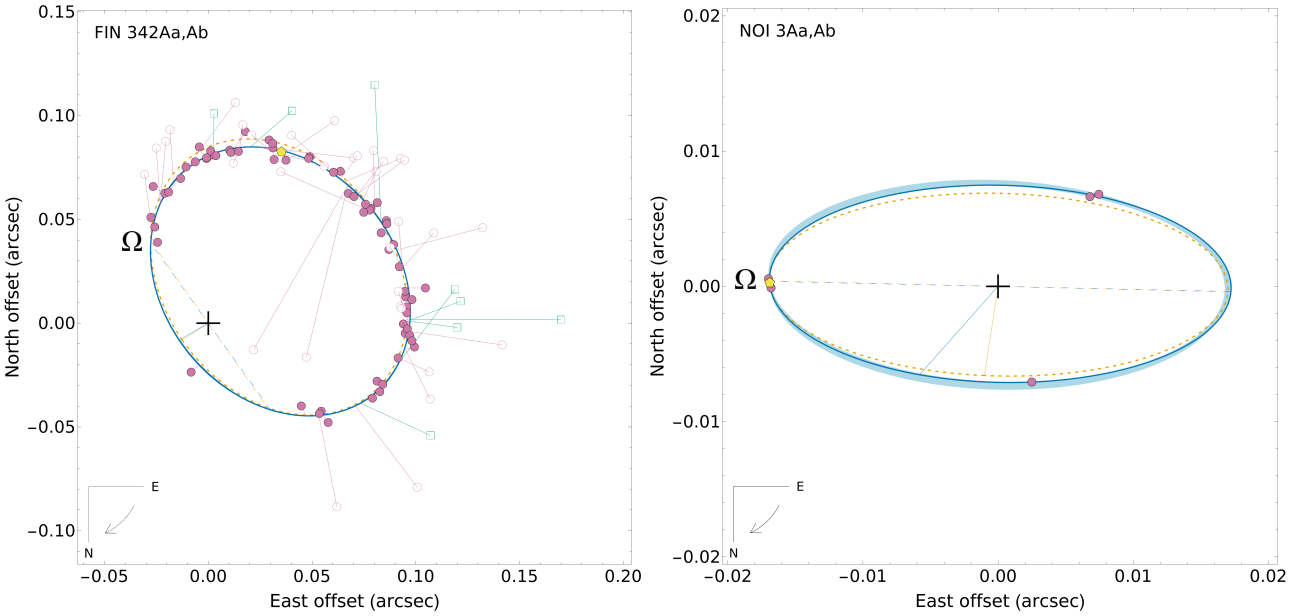

Fig. 4. Optimised apparent orbits of FIN 342Aa,Ab and NOI 3Aa,Ab. The new orbit (solid dark blue line) and the previous one (dashed orange line) are plotted together with the available measurements. Micrometric and interferometric observations are shown as filled green squares and magenta circles, respectively, while measurements identified as outliers (and therefore excluded from the fit) are displayed as empty geometric shapes. The most recent observation is represented by a yellow pentagon. Thick solid lines connect each observation to its corresponding calculated position along the new orbit. The dashed blue line marks the new line of nodes (with Ω indicating the ascending node), and the solid blue line indicates the direction of periastron; both are shown in orange for the previous orbit. The light blue area represents the uncertainty region derived from the jackknife procedure as described in Sect. 3.3 (that representing the orbital uncertainty of FIN 342AaAb is not visible at this scale because it is too small).

4.2. Case 2: 22 Cas A (NOI 3Aa,Ab/WDS 00447+4817)

This is a triple stellar system whose primary component, 22 Cas A, is a bright classical Be star. As noted by Hubert-Delplace & Hubert (1979), it exhibits recurrent transitions between B-star and Be-star phases, and according to Banerjee et al. (2022) it may currently be undergoing disc-loss episodes. Its spectral classification has varied considerably in the literature, ranging from B5 III, B2 V, and B3 IV to B2 V.

Abt & Levy (1978) reported that the primary is itself a single-lined spectroscopic binary (SB1) and provided orbital elements based on observations covering a single cycle. The SB1 nature of the system was subsequently called into question by Harmanec (1987). However, the system was also subsequently resolved interferometrically by Koubský et al. (2010), who identified the binary as NOI 3Aa,Ab. A third component, 22 Cas B, lies at much wider separation.

Using their interferometric measurements, Koubský et al. (2010) derived the inclination (i), the position angle of the ascending node (Ω), and the semi-major axis (a), adopting the remaining elements from the spectroscopic orbit. A full visual orbit was later provided by Docobo & Campo (2019), but the resulting orbit shows substantial residuals, making this system a particularly suitable test case for assessing the performance of our framework.

The orbit presented in this research has been derived from the interferometric measurements reported by Koubský et al. (2010), which remain the only astrometric data available for this subsystem. Although these interferometric observations have been used previously to compute orbital solutions, earlier analyses did not fully exploit the complete astrometric information. The improved solution obtained here, based on a more comprehensive treatment of the data, is therefore of particular interest.

4.2.1. Robust analysis: Outliers and leverage points

The six optical-interferometric measurements span approximately two thirds of the full orbital period. The `ANAorb` outlier analysis detected neither leverage points nor vertical outliers, and all data points, which are distributed over three well-separated orbital arcs, were retained in the computation of the best-fit solution. Moreover, the dataset follows a normal distribution, as confirmed by the normality test introduced in Sect. 3.1.2. The outlier map is shown in Fig. C.1.

4.2.2. New orbital elements

The presently adopted orbit of NOI 3Aa,Ab (Docobo & Campo 2019) is classified as 'good' in ORB6 catalogue. Our revised orbit, however, provides a markedly better representation of the data.

We calculated new orbital elements (see Table 3). In this case the ascending node can be identified due to its spectroscopic feature. This optimised apparent orbit is shown in Fig. 4.

In terms of accuracy, the new orbit yields lower MAE and RMSE values for the Euclidean distance and for both θ and ρ, as listed in Table C.1. Moreover, according to the dimensionless accuracy factors introduced in Sect. 3.4, the solution can be regarded as moderately constrained ($\Gamma = 0.7007$). Additional high-precision interferometric observations would therefore be desirable, although the system was reported as single in several 4 m class observations by Mason et al. (1997, 2009). In any case, the residuals of the new orbit are substantially reduced with respect to the previous solution.

The case examined demonstrates that three-point orbit-determination algorithms, exemplified by that of Docobo (1985), can become trapped in suboptimal regions of parameter space

when applied to the orbital fitting of visual binaries. Although the algorithm yielded a set of orbital elements formally consistent with its internal computational scheme, and differential corrections were applied, subsequent analysis revealed that the resulting solution did not correspond to the global minimum, nor did it reproduce the true apparent motion of the system with adequate accuracy.

The failure arises from the strong dependence of such algorithms on the chosen initial measurements and from their reliance on locally linearised differential corrections. Under these circumstances, it became trapped within a local basin of attraction, converging towards a set of parameters that minimised the discrepancies between observed and modelled positions only in a local sense. However, when the same problem is approached using global optimisation techniques, it becomes evident that there exist regions of the parameter space that provide a substantially better fit to the astrometric data.

4.2.3. Dynamical parallax and individual masses

The combined G magnitude reported for this system in the *Gaia* DR3 catalogue is 4.3495 ± 0.0041. However, given the well-known brightness variability produced by the circumstellar disc of the Be primary, this value is likely overestimated by approximately 0.3 mag. To mitigate this effect, we examined the historical photometric record to identify epochs when the disc contribution was minimal. The faintest measurements, which we adopt as representative of the photospheric brightness (star without emission), correspond to $m = 4.61 \pm 0.03$ (Haupt & Schroll 1974). In addition, the magnitude difference derived from the optical-interferometric observations of Koubský et al. (2010) is $\Delta m = 2.9 \pm 0.1$. Combining these values yields individual apparent magnitudes of 4.68 ± 0.03 and 7.58 ± 0.10 for the primary and secondary components, respectively.

The trueness of these magnitudes, together with the well-determined orbital period and semi-major axis, enables robust estimates of the dynamical parallax and individual stellar masses through `ANApar` (see Table 3). The resulting dynamical parallax, 3.622 ± 0.043 mas, is significantly larger than the most recent trigonometric parallax reported in *Gaia* DR3, 0.51 ± 0.73 mas, with a RUWE of 3. This value clearly suffers from poor astrometric quality, most likely because of variability, the presence of a Be disc, and binarity (as noted for the previous example). In contrast, our dynamical parallax is fully consistent with the HIPPARCOS measurement of 3.60 ± 0.82 mas (Perryman et al. 1997).

The individual masses inferred for the components (see Table 3) are fully compatible with two main-sequence stars of approximate spectral types B2 and B8, in agreement with the combined spectral classification B2 V. These masses are likewise consistent with those expected for a pair of B-type stars exhibiting a magnitude difference of 2.9 mag. Moreover, the parallax derived in this study implies an extinction-corrected absolute magnitude of -2.69 ± 0.05 for the primary component. According to standard luminosity calibrations (e.g. Pecaut & Mamajek 2013; Xia & Fu 2010; Straizys & Kuriliene 1981), this value corresponds to a B1.5 V–B2 V star with an estimated mass of roughly 7–11 $\mathcal{M}_\odot$. Consequently, it appears unlikely that the long-standing discrepancy in mass estimates can be resolved by assuming that the secondary is itself an unresolved close binary (Koubský et al. 2010). Rather, the evidence compellingly suggests that both components, especially the primary, are intrinsically massive B-type stars. Consequently, this emerges as the only hypothesis that consistently reconciles the photometric, spectroscopic, and astrometric datasets.

5. Summary and conclusions

In this work, we introduced `ANAorb`, a robust and flexible framework for determining orbital solutions for visual binary systems by means of an optimisation algorithm designed to obtain the statistically most favourable local minimum (maybe the global minimum) of the model's objective function. Although initially implemented in Mathematica, the methodology is general and can be ported to other programming environments with minimal adaptation.

`ANAorb` automatically handles the various epochs (Besselian or Julian), unit conventions (years or days), and quadrant assignments of heterogeneous astrometric datasets, and applies the appropriate corrections for extinction and atmospheric refraction. A key component of the framework is its robust statistical treatment of the input data. Outliers are identified and rejected through objective statistical diagnostics, which ensures that the resulting orbital solutions are not biased by spurious measurements. This greatly enhances the reliability of the final orbital parameters, especially when working with long historical time series.

The seven-dimensional parameter space of the orbital elements is exhaustively explored through a search aimed at locating the global minimum of an objective function defined in terms of the Euclidean distance between observed and computed positions. This is achieved by employing a suite of optimisation algorithms, both global and local, and either derivative-based or derivative-free, which collectively ensure reliable convergence towards the optimised set of orbital elements.

The uncertainties of the orbital elements are estimated via a jackknife resampling procedure, in which each observation is systematically omitted and the orbit recomputed. The scatter among the jackknife realisations provides a model-independent and statistically robust estimate of the uncertainties.

To assess the overall accuracy of the orbital solutions, we defined new quantities that measure both trueness and precision. These provide a neutral framework for comparing orbital solutions obtained for different systems or from different datasets.

Finally, we incorporated the rigorous dynamical-parallax formulation provided by `ANApar` (Andrade 2019) into the modelling framework, which enabled the derivation of accurate dynamical parallaxes and individual masses directly from the optimised orbital solution.

We illustrated the capabilities of `ANAorb` on two representative binaries and obtained markedly improved orbits, distances, and masses. However, the primary goal of this work was to introduce and validate the `ANAorb` framework. Its application to a larger sample will be presented in a subsequent publication.

Future developments of `ANAorb` will aim to incorporate additional observables into the current deterministic optimisation framework, in particular radial velocity measurements and forthcoming *Gaia* astrometric time series. A central goal will be to preserve the robustness, automated outlier rejection, and low computational cost that characterise the present implementation.

Data availability

The code presented in this paper, together with the example input files needed to reproduce the calculations discussed here, is publicly archived on Zenodo. The archived release, v1.0.0, is available at `doi:10.5281/zenodo.20172758`.

Acknowledgements. I warmly thank Miguel E. Vázquez-Méndez for his valuable suggestions and for the inspiring discussions we have shared. The author thanks the anonymous referee for a careful review and constructive suggestions. This research has made use of the SIMBAD database, CDS, Strasbourg Astronomical Observatory, France. This research has made use of the Astrophysics Data System, funded by NASA under Cooperative Agreement 80NSSC21M00561. This research has made use of the Washington Double Star Catalog maintained at the U.S. Naval Observatory. This work has made use of data from the European Space Agency (ESA) mission HIPPARCOS (https://www.cosmos.esa.int/web/hipparcos). This work has made use of data from the European Space Agency (ESA) mission *Gaia* (https://www.cosmos.esa.int/gaia), processed by the *G*aia Data Processing and Analysis Consortium (DPAC, https://www.cosmos.esa.int/web/gaia/dpac/consortium). Funding for the DPAC has been provided by national institutions, in particular the institutions participating in the *G*aia Multilateral Agreement. This research has used data, tools or materials developed as part of the EXPLORE project that has received funding from the European Union's Horizon 2020 research and innovation programme under grant agreement No 101004214. This paper was supported by the Spanish *Agencia Estatal de Investigación* under the project PID2021-122608NB-I00.

References

Abt, H. A., & Levy, S. G. 1978, ApJS, 36, 241
Andrade, M. 2019, A&A, 630, A96
Banerjee, G., Mathew, B., Paul, K. T., et al. 2022, JApA, 43, 102
Benedict, G. F., Henry, T. J., Franz, O. G., et al. 2016, AJ, 152, 141
Blunt, S., Wang, J. J., Angelo, I., et al. 2020, AJ, 159, 89
Brandt, T. D., Dupuy, T. J., Li, Y., et al. 2021, AJ, 162, 186
Brent, R. P. 1973, Algorithms for Minimization Without Derivatives, Dover Books on Mathematics (Dover Publications)
Broyden, C. G. 1970, IMA J. Appl. Math., 6, 222
Černý, V. 1985, J. Optim. Theory Appl., 45, 41
Cid, R. 1958, AJ, 63, 395
Davidon, W. C. 1991, SIAM J. Optim., 1, 1
Docobo, J. A. 1985, Celest. Mech., 36, 143
Docobo, J. A., & Campo, P. P. 2019, Double Star Inf. Circ., 197, 1
Dupuy, T. J., & Liu, M. C. 2017, ApJS, 231, 15
Efron, B. 1982, The Jackknife, the Bootstrap and other resampling plans (CBMS-NSF Regional Conference Series in Applied Mathematics, Philadelphia: Society for Industrial and Applied Mathematics) (SIAM)
Fan, S.-K. S., & Zahara, E. 2007, Eur. J. Oper. Res., 181, 527
Finsen, W. S. 1959, Circ. Union Obser. Johannesburg, 118, 315
Fletcher, R. 1970, Comput. J., 13, 317
Goldfarb, D. 1970, Math. Comp., 24, 23
Gray, R. O., Napier, M. G., & Winkler, L. I. 2001, AJ, 121, 2148
Griffin, R. F. 2012, JApA, 33, 29
Harmanec, P. 1987, Bull. Astron. Inst. Czech., 38, 283
Hartkopf, W. I., McAlister, H. A., & Franz, O. G. 1989, AJ, 98, 1014
Hartkopf, W. I., McAlister, H. A., & Franz, O. G. 1992, AJ, 104, 810
Hartkopf, W. I., Mason, B. D., & Worley, C. E. 2001a, AJ, 122, 3472
Hartkopf, W. I., McAlister, H. A., & Mason, B. D. 2001b, AJ, 122, 3480
Haupt, H. F., & Schroll, A. 1974, A&AS, 15, 311
Heintz, W. D. 1978, Double Stars, Geophysics and Astrophysics Monographs (Springer Netherlands)
Herschel, W. 1803, Phil. Trans. R. Soc. Lond. I, 93, 339
Hestenes, M. R., & Stiefel, E. 1952, J. Res. Natl. Bur. Stand., 49, 409
Hinkley, D. V. 1978, Biometrika, 65, 13
Horch, E. P., Broderick, K. G., Casetti-Dinescu, D. I., et al. 2021, AJ, 161, 295
Hubert-Delplace, A.-M., & Hubert, H. 1979, An Atlas of Be Stars
Jarque, C. M., & Bera, A. K. 1981, Econ. Lett., 7, 313
Kirkpatrick, S., Gelatt, C. D., & Vecchi, M. P. 1983, Science, 220, 671
Koubský, P., Hummel, C. A., Harmanec, P., et al. 2010, A&A, 517, A24
Kowalsky, M. 1873, in Proceedings of the Kasan Imperial University (Kazan: Kasan Imperial University)
Lallement, R., Vergely, J. L., Babusiaux, C., & Cox, N. L. J. 2022, A&A, 661, A147
Le Contel, D., Valtier, J.-C., & Bonneau, D. 2001, A&A, 377, 496
Malkov, O. Y., & Sachkov, A. M. 2025, Galaxies, 13, 96
Mason, B. D., & Hartkopf, W. I. 2026, AJ, 171, 149
Mason, B. D., ten Brummelaar, T., Gies, D. R., Hartkopf, W. I., & Thaller, M. L. 1997, AJ, 114, 2112
Mason, B. D., Hartkopf, W. I., Gies, D. R., Henry, T. J., & Helsel, J. W. 2009, AJ, 137, 3358
McAlister, H. A., Hartkopf, W. I., Bagnuolo, Jr., W. G., et al. 1988, AJ, 96, 1431
Mendez, R. A., Claveria, R. M., Orchard, M. E., & Silva, J. F. 2017, AJ, 154, 187
Metropolis, N., Rosenbluth, A. W., Rosenbluth, M. N., Teller, A. H., & Teller, E. 1953, J. Chem. Phys., 21, 1087
Moré, J. J., & Thuente, D. J. 1994, ACM Trans. Math. Softw., 20, 286
Nelder, J. A., & Mead, R. 1965, Comput. J., 7, 308
Parenago, P. P. 1945, Popul. Astron., 53, 441
Pecaut, M. J., & Mamajek, E. E. 2013, ApJSS, 208, 9
Perryman, M. A. C., Lindegren, L., Kovalevsky, J., et al. 1997, A&A, 323, L49
Polak, E., & Ribière, G. 1969, Rev. Franç. Inform. Rech. Opér., 3, 35
Pourbaix, D. 1994, A&A, 290, 682
Price, K., Storn, R. M., & Lampinen, J. A. 2005, Differential Evolution, Natural Computing Series (Springer-Verlag Berlin Heidelberg)
Quenouille, M. H. 1949, Ann. Math. Stat., 20, 355
Reino, S., de Bruijne, J., Zari, E., d'Antona, F., & Ventura, P. 2018, MNRAS, 477, 3197
Rousseeuw, P. 1985, Multivariate Estimation with High Breakdown Point, Mathematical Statistics and Applications, Proc. 4th Pannonian Symp. Math. Stat., Bad Tatzmannsdorf/Austria 1983, Vol. B, 283
Rousseeuw, P. J. 1984, J. Am. Stat. Assoc., 79, 871
Rousseeuw, P. J., & Driessen, K. V. 1999, Technometrics, 41, 212
Rousseeuw, P. J., & Leroy, A. M. 1987, Robust Regression and Outlier Detection, Wiley Series in Probability and Mathematical Statistics. Applied Probability and Statistics (John Wiley & Sons, Inc.)
Rousseeuw, P. J., & van Zomeren, B. C. 1990, J. Am. Statist. Assoc., 85, 633
Savary, M. 1830, Connaissance des Temps, 163
Shanno, D. F. 1971, Math. Comput., 24, 647
Shao, J., & Wu, C. F. J. 1989, Ann. Stat., 17, 1176
Shapiro, S. S., & Wilk, M. B. 1965, Biometrika, 52, 591
Sharov, A. S. 1964, Soviet Ast., 7, 689
Söderhjelm, S. 1999, A&A, 341, 121
Storn, R., & Price, K. 1997, J. Glob. Optim., 11, 341
Straizys, V., & Kuriliene, G. 1981, Ap&SS, 80, 353
Thiele, T. N. 1883, Astron. Nachr., 104, 245
Thompson, W., Lawrence, J., Blakely, D., et al. 2023, AJ, 166, 164
Tokovinin, A. 2016, Zenodo
Tokovinin, A. 2024, AJ, 168, 190
Tokovinin, A., Mason, B. D., Hartkopf, W. I., Mendez, R. A., & Horch, E. P. 2018, AJ, 155, 235
Tokovinin, A., Mason, B. D., Mendez, R. A., Horch, E. P., & Briceño, C. 2019, AJ, 158, 48
Tokovinin, A., Mason, B. D., Mendez, R. A., & Costa, E. 2022, AJ, 164, 58
Torres, G., Stefanik, R. P., & Latham, D. W. 1997, ApJ, 479, 268
Tukey, J. W. 1958, Ann. Math. Statist., 29, 614
van den Bos, W. H. 1926, Circ. Union Obser. Johannesburg, 68, 352
van den Bos, W. H. 1932, Circ. Union Obser. Johannesburg, 86, 261
van Leeuwen, F. 2007, A&A, 474, 653
Xia, F., & Fu, Y.-N. 2010, Chinese Astron. Astrophys., 34, 277

Appendix A: Keplerian model for visual binary-star orbits

A.1. Thiele-Innes representation

The orbit of a purely visual binary (i.e. with relative astrometric measurements only), it is usually described in terms of the classical Campbell elements (P, T, e, a, i, Ω, and ω). However, for orbit determination from relative astrometry, it is often advantageous to re-parametrise the last four elements in terms of the Thiele-Innes constants:

$$\begin{aligned} A &= a\,(\cos\omega\cos\Omega - \sin\omega\sin\Omega\cos i)\,,\\ B &= a\,(\cos\omega\sin\Omega + \sin\omega\cos\Omega\cos i)\,,\\ F &= a\,(-\sin\omega\cos\Omega - \cos\omega\sin\Omega\cos i)\,,\\ G &= a\,(-\sin\omega\sin\Omega + \cos\omega\cos\Omega\cos i)\,. \end{aligned} \tag{A.1}$$

These are more suited to work with the Cartesian coordinates in the apparent orbital plane:

$$\begin{cases} x(t) = A\,X(t) + F\,Y(t),\\ y(t) = B\,X(t) + G\,Y(t), \end{cases} \tag{A.2}$$

where $X(t)$ and $Y(t)$ are the normalised Cartesian coordinates in the true orbital plane:

$$\begin{cases} X(t) = \cos E(t) - e,\\ Y(t) = \sqrt{1-e^2}\,\sin E(t), \end{cases} \tag{A.3}$$

$E(t)$ being the eccentric anomaly.

A.2. Kepler's equation and motion in the orbital plane

Given the period P and epoch of periastron T_0, the mean motion is

$$n = \frac{2\pi}{P}\,, \tag{A.4}$$

and the mean anomaly at time t is

$$M(t) = n\,(t - T). \tag{A.5}$$

The eccentric anomaly (E) is then defined implicitly by Kepler's equation

$$M = E - e\sin E\,. \tag{A.6}$$

For each t_i we solved Eq. (A.6) numerically, for example by using a Newton-Raphson iteration with a suitable initial guess. This step is computationally inexpensive and well behaved for $0 \leq e < 1$.

A.3. Parameter correlations and degeneracies

The Keplerian model described above is conceptually simple but exhibits strong parameter correlations and well-known degeneracies in practice. Examples particularly relevant for visual binaries include:

- For nearly circular orbits ($e \approx 0$), the argument of the periastron ω cannot be determined (or becomes extremely poorly constrained), because the periastron direction becomes undefined.
- For nearly face-on systems ($i \approx 0°$), the node Ω cannot be determined (or becomes extremely poorly constrained), because all values of Ω produce essentially the same sky projection.
- Because a reflection of the true orbit across the plane of the sky leaves the projected ellipse unchanged, the node ambiguity ($\Omega \rightarrow \Omega + 180°$) cannot be addressed using relative astrometry; only radial velocities allow the ascending node to be determined.
- The coupling between a and i when the orbit is only partially covered since a smaller semi-major axis seen at lower inclination can mimic a larger, more edge-on orbit.

These features strongly motivate the use of global exploration strategies as those presented in this research.

Appendix B: Optimisation algorithms

The following list outlines the key optimisation methods and their parameters employed to obtain optimised orbital solutions using `ANAorb`. These methods are designed to efficiently explore the parameter space, minimise residuals, and ensure that the resulting orbits provide the most accurate representation of the observational data.

Nelder-Mead simplex (NM): This is a direct search algorithm for non-linear optimisation problems making no use of the objective function derivatives (Nelder & Mead 1965).
We intend to use a 7-simplex, a geometric object that is the convex hull of 8 points in $\mathbb{R}^7$ not lying in the same hyperplane. The method search for new solutions using a sequence of reflections, expansions, contractions, and shrinks of the extreme point with the worst function value through the centroid of the remaining extreme points. As result, the worst vertex is replaced by a better one after each transformation.
`ANAorb` allows us to choose the control parameters used for each one of these operations, specifically, the constant factors of reflection α, contraction β, expansion γ, and shrinking δ. Otherwise, it takes those values recommended by Fan & Zahara (2007) as default.

Simulated annealing (SA): This is a stochastic global search algorithm for non-linear optimisation problems that avoids getting trapped in local minima. It simulates the thermodynamic process of slow cooling of a system of particles (Metropolis et al. 1953) to achieve the minimum function value in a minimisation problem (Kirkpatrick et al. 1983; Černý 1985).
It operates iteratively by generating a new state $\tilde{\mathbf{x}}$ from a neighbourhood of the current state $\mathbf{x}$. The probability function, $P(\mathbf{x}, \tilde{\mathbf{x}}, T)$, of accepting $\tilde{\mathbf{x}}$ to replace, or not, $\mathbf{x}$, is controlled by the temperature (T; by analogy to the physical cooling process). The values of the latter depend on the choice of the cooling schedule, which is determined by the cooling ratio (α) and the number of iterations at each step, called the epoch length L. As usual, the default probability is the well-known Metropolis acceptance probability,

$$P(\mathbf{x}, \tilde{\mathbf{x}}, T) := \begin{cases} 1 & \text{if } f(\tilde{\mathbf{x}}) \leq f(\mathbf{x}),\\ e^{\dfrac{f(\tilde{\mathbf{x}}) - f(\mathbf{x})}{T}} & \text{if } f(\tilde{\mathbf{x}}) > f(\mathbf{x}). \end{cases} \tag{B.1}$$

However, `ANAorb` also allows us to use a different probability function as well as to freely configure the parameters of the cooling schedule.

Differential evolution (DE): This is an evolutionary algorithm on the basis of genetic strategies used in non-linear global optimisation problems (Storn & Price 1997).
We consider a population of N points, with $N \gg 7$. First,

considering an initial point of this population, the mutation operation gives us a new point that is generated considering three randomly chosen points. The diversity of the new population is guaranteed by the crossover operation which mixes this mutant point with the initial point. Finally, the selection operation determines whether the initial point must be replaced by the new point depending on which of them yields the best objective function value.

`ANAorb` allows us to choose the control parameters, namely the mutation scale factor (F), the crossover constant (C_r), and the size of the population used for evolution (N_p). These parameters have a great impact on the quality of the expected optimal value as well on the rate of convergence but, unfortunately, it is not easy to select effective control parameters. Anyway, as a rule of thumb, we can select those values indicated by Price et al. (2005).

Principal axis (PA): This is an adaptive coordinate descent algorithm, also known as Brent's algorithm (Brent 1973). As a derivative-free method it builds up an approximate model assuming quadratic form of the optimised function and repeatedly updating a set of conjugate search directions.

Interior point (IP): This non-linear search method for constrained local optimisation requires first and second derivatives of the objective and constraints. A barrier term is added to the objective function to account for non-negative constrictions, as those given in Eq. (11). In addition, the Karush-Kuhn-Tucker conditions, analogous to the condition that the gradient must be zero at a minimum, must be met.

Newton (Nw): The Newton's method of calculus tries to find the roots of the equation $f(\mathbf{x}) = 0$ from an initial point $\mathbf{x}_0$ by constructing a sequence $\mathbf{x}_k$ that converges towards some value $\mathbf{x}^*$ satisfying $\nabla f(\mathbf{x}^*) = 0$. Such $\mathbf{x}^*$ is a stationary point of $f(\mathbf{x})$. When this method is used for minimisation of the function $f(\mathbf{x})$ we try to find the root of the function $g = \nabla f(\mathbf{x})$. Thus, assuming that $f(\mathbf{x})$ is twice differentiable, the necessary (and sufficient for f convex) condition for minimisation is given by the first-order system $\nabla f(\mathbf{x}) = 0$, whose solutions are given by the iterative equation

$$\mathbf{x}_{k+1} = \mathbf{x}_k - \left[\nabla^2 f(\mathbf{x}_k)\right]^{-1} \nabla f(\mathbf{x}_k), \tag{B.2}$$

where $H(\mathbf{x}_k) \equiv \nabla^2 f(\mathbf{x}_k)$ is the Hessian matrix. Thus, $\mathbf{x}_0$ will be a local minimum if the gradient is zero and $H(\mathbf{x}_0)$ is positive definite.

There are two fundamental strategies that allow to decide how to move from the current point $\mathbf{x}_k$ to a new iterate $\mathbf{x}_{k+1}$: line search and trust region. `ANAorb` allows us to implement both of them. Given the step direction $d_k = -\left[\nabla^2 f(\mathbf{x}_k)\right]^{-1} \nabla f(\mathbf{x}_k)$, the line search decides how far to move along that direction considering the so-called damped Newton's method,

$$\mathbf{x}_{k+1} = \mathbf{x}_k - \alpha_k \left[\nabla^2 f(\mathbf{x}_k)\right]^{-1} \nabla f(\mathbf{x}_k), \tag{B.3}$$

where the step length $0 < \alpha_k \leq 1$ is chosen to achieve a monotone decrease in $\|\nabla f(\mathbf{x}_k)\|$ and, therefore, convergence in fewer iterations. The latter, trust region, modifies step lengths by using a linear approximation of $\nabla f(\mathbf{x}_k)$ where this is valid.

Quasi-Newton (QNw): Davidon (1991) developed in the mid 1950s the first quasi-Newton method for which the Hessian matrix does not need to be directly evaluated. Therefore, although not as robust as Newton-type methods, quasi-Newton methods can be more efficient. The most popular and efficient quasi-Newton algorithm is the Broyden-Fletcher-Goldfarb-Shanno (BFGS) method (Broyden 1970; Fletcher 1970; Goldfarb 1970; Shanno 1971).

Analogously to the Newton's method, the search direction at a stage k is given by $d_k = -\left[\tilde{H}_k\right]^{-1} \nabla f(\mathbf{x}_k)$, where $\tilde{H}_k$ in some approximation to the Hessian $\nabla^2 f(\mathbf{x}_k)$. This is approximated at each iteration using information from the values of the function and the gradient in agreement with the equation

$$\tilde{H}_{k+1}=\tilde{H}_k - \frac{\delta_k \gamma_k^T \tilde{H}_k + \tilde{H}_k \gamma_k \delta_k^T}{\delta_k^T \gamma_k} + \left(1+\frac{\gamma_k^T \tilde{H}_k \gamma_k}{\delta_k^T \gamma_k}\right)\frac{\delta_k \delta_k^T}{\delta_k^T \gamma_k}, \tag{B.4}$$

where we defined the vectors

$$\begin{cases} \delta_k = \mathbf{x}_{k+1} - \mathbf{x}_k, \\ \gamma_k = \nabla f(\mathbf{x}_{k+1}) - \nabla f(\mathbf{x}_k), \end{cases} \tag{B.5}$$

such that the next approximation matrix, $\tilde{H}_{k+1}$, must satisfy the secant equation $\tilde{H}_{k+1}\gamma_k = \delta_k$.

`ANAorb` allows us to select the effective number of steps to store in the Hessian approximation, thus avoiding a costly storage, as well as to decide whether to use a line search strategy or not.

Levenberg-Marquardt (LM): This is an iterative algorithm for non-linear least-squares optimisation. It can be understood as a damped version of the Gauss-Newton method, combining its fast convergence near a minimum with the greater robustness of gradient descent. At each iteration, the residuals are locally linearised using their Jacobian, giving a quadratic approximation to the sum-of-squares objective. A damping parameter controls the step: when it is small, the method behaves like Gauss-Newton; when it is large, it behaves more like gradient descent. For this reason, LM is especially useful for fitting non-linear models to data, which is precisely the type of problem considered here.

Conjugate gradient (CG): This is an iterative algorithm for finding the nearest local minimum of a function (Hestenes & Stiefel 1952) which tries to improve the behaviour of the steepest descent method by partially considering the previous direction to the current negative gradient direction as

$$d_k = -\nabla f(\mathbf{x}_k) + \beta_k\, d_{k-1}. \tag{B.6}$$

We chose the scalar β_k to be that given by the formula of Polak & Ribière (1969) for non-linear functions

$$\beta_k = \frac{\left[\nabla f(\mathbf{x}_{k-1}) - \nabla f(\mathbf{x}_k)\right]^T \nabla f(\mathbf{x}_k)}{\left[\nabla f(\mathbf{x}_{k-1})\right]^T \nabla f(\mathbf{x}_{k-1})}. \tag{B.7}$$

`ANAorb` allows us to restart the method after a certain number of iterations or when consecutive gradients are not orthogonal according to the test

$$\frac{|\,\nabla f(\mathbf{x}_k)\cdot\nabla f(\mathbf{x}_{k-1})\,|}{\nabla f(\mathbf{x}_k)\cdot\nabla f(\mathbf{x}_k)} < \nu, \tag{B.8}$$

with $0 < \nu < 1$.

Regarding Newton and gradient-based methods, `ANAorb` can run three line search algorithms to determine the direction along which to search a suitable point that would lead to convergence, that of Moré & Thuente (1994), backtracking and that of Brent (1973). In addition, `ANAorb` also implements the very simple and quite effective Armijo backtracking line search where each backtracking step is derived from a polynomial interpolation with backtracking parameters $0 < c_1 \leq c_2 < 1$.

Appendix C: Additional material for the illustrative examples discussed in Sect. 4

The distribution of outliers identified by the robust fitting procedure is shown in Fig. C.1 with separate panels for FIN 342Aa,Ab (70 Tau) and NOI 3Aa,Ab (22 Cas A). A quantitative assessment of the corresponding orbital solutions is presented in Table C.1, which reports the classical error metrics (MAE and RMSE) for the polar coordinates and the Euclidean separation, together with the newly introduced normalised trueness (Φ) and precision (Θ) factors, as well as the accuracy index (Γ).

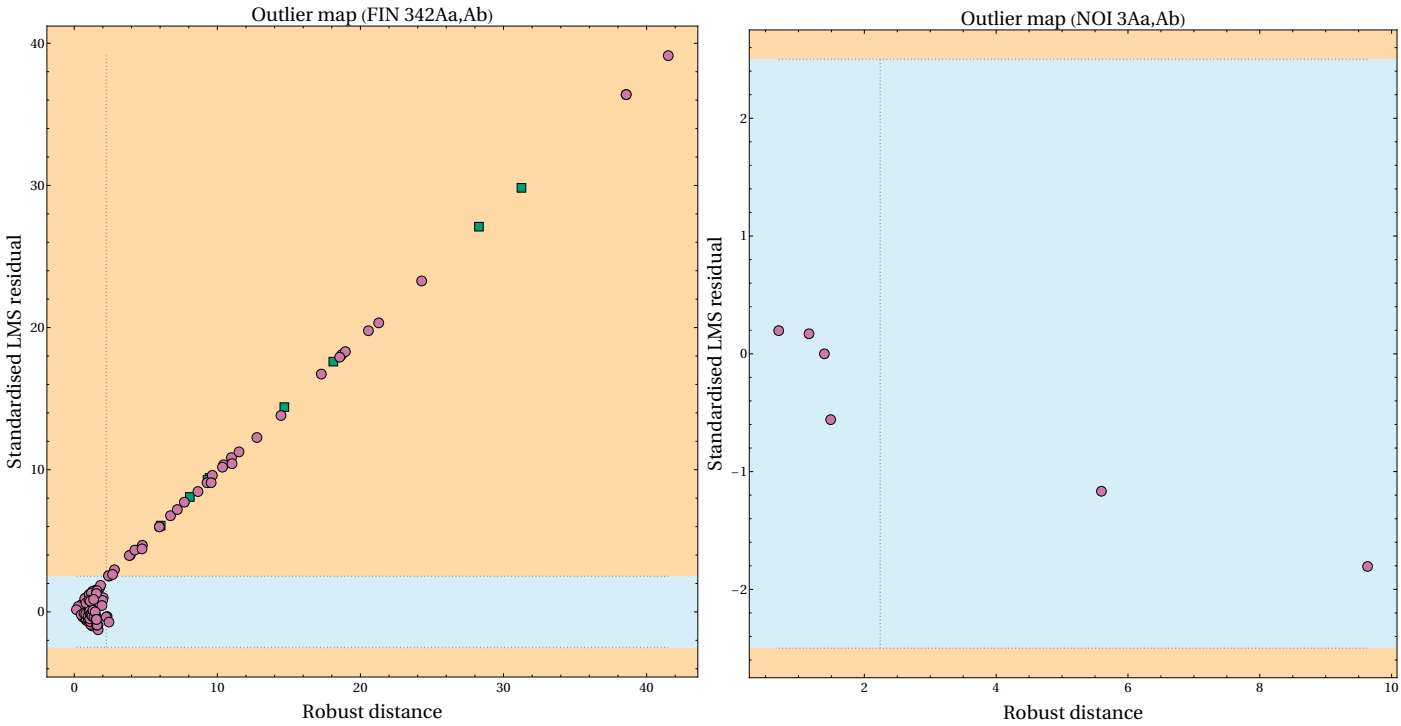

Fig. C.1: Outlier maps for the measurements of FIN 342Aa,Ab (70 Tau) and NOI 3Aa,Ab. Micrometric and interferometric observations are shown as filled green squares and magenta circles, respectively. Regions are coloured following the colour scheme shown in Fig. 1.

Table C.1: Evaluation of the orbital solution of FIN 342Aa,Ab and NOI 3Aa,Ab.

	FIN 342Aa,Ab				NOI 3Aa,Ab			
Classical metrics	(1)		This work		(2)		This work	
	MAE	RMSE	MAE	RMSE	MAE	RMSE	MAE	RMSE
θ (deg)	+2.48	4.44	+1.81	4.15	+0.44	0.51	+0.42	0.48
ρ (mas)	+4.07	7.23	+3.60	7.11	+0.37	0.51	+0.11	0.15
d (mas)	+4.76	5.24	+2.87	3.44	+0.42	0.52	+0.17	0.19
New factors of evaluation	(1)		This work		(2)		This work	
Φ	0.7023		0.7023		0.0892		0.0890	
Θ	0.0000		0.9827		0.0000		0.9870	
Γ	0.4966		0.8541		0.0631		0.7007	

Notes. The upper part presents the classical mean absolute error (MAE) and root mean square error (RMSE) for the coordinates (θ, ρ) and for the Euclidean distance d. The lower part summarises the new normalised trueness factor Φ, precision factor Θ, and accuracy index Γ.
References. (1) Söderhjelm (1999); (2) Docobo & Campo (2019).